2026 European Control Conference (ECC)
July 7-10, 2026. Reykjavík, Iceland

Airborne Wind Energy: The KEEP Project*

Antonin Bavoil,[1,†] Jean-Baptiste Caillau,[1] Lamberto Dell'Elce[2] and Alain Nême[3]

***Abstract*— A ground-generation airborne wind energy system is considered. The device consists of a kite attached to an oscillating arm in the horizontal plane that generates electricity. The kite's trajectory is constrained to follow a prescribed lemniscate pattern. An implicit modeling approach is adopted where the control force required to maintain the figure-eight trajectory is computed. This system is reduced to a two-dimensional second-order ordinary differential equation. Its limit cycles are studied numerically, with specific equilibria serving as starting points to obtain physically admissible periodic motions. These cycles depend on several design parameters including line length, arm inertia, and braking coefficient, that are tuned to maximize the average power generated by the arm's oscillations. The system's behavior is further analyzed across a typical range of wind speeds, demonstrating robustness to wind variations while maintaining positive line tension throughout the cycle.**

I. INTRODUCTION

This work is aimed at improving the performance of technologies that meet challenges of the energy transition. The innovative KEEP (Kite Electrical Energy Production) technology developed at ENSTA enables the production of electrical energy from a kite capturing wind energy. It is a Ground-Gen system with a moving ground station (rocking arm) simpler than the devices described, *e.g.*, in [2]. The first numerical models of the system show an increase of about 50% in the efficiency of this technology compared to already existing ones [4]. In the short and medium term, onshore and shipboard applications with a power production ranging from a few tens to hundreds of kW are targeted, with an extension to an offshore production capacity at a MW scale with 1000 m^2 kites. To this end, the following developments are required: the improvement of the mechanical model, as well as the theoretical analysis and optimization of the complete dynamical system.

The paper is organized as follows: in Section II we present a brief derivation of the model. Our approach consists of an implicit modeling of the control exerted on the kite: we compute the force such that the motion is indeed prescribed to a figure-eight trajectory, typical of the desired motion. While the resulting system is a differential algebraic equation (DAE), it is possible to make it explicit as a two-dimensional second-order ODE. We are interested in the limit cycles of this equation, and study them numerically in Section III. In order to obtain the relevant periodic motion (only some limit cycles are admissible for the kite), it is convenient to initialize the ODE solver near an equilibrium with a carefully chosen velocity; therefore, we study the equilibria of the dynamical system. The resulting limit cycle, that depends on several design parameters, is then optimized so as to maximize the energy generated by the motion (the kite is attached to an arm in the ground plane whose oscillations feed a generator). This optimization with respect to a set of finite dimensional parameters is discussed in Section IV and leads to an approximate 13% increase of the generated power.

*Work was supported by CNRS funding.

[1]Université Côte d'Azur, CNRS, Inria, LJAD antonin.bavoil@univ-cotedazur.fr, jean-baptiste.caillau@univ-cotedazur.fr.
[2]Université Côte d'Azur, Inria, CNRS, LJAD lamberto.dellelce@inria.fr.
[3]ENSTA, Institut Polytechnique de Paris, CNRS, IRDL alain.neme@ensta.fr.

II. MODEL

A. Geometry and Generalized Coordinates

The device we model is composed of an electric generator at O, a rigid arm of length a that rotates in the horizontal plane attached to the generator and ending in A, and a kite K positioned at distance ℓ, the length of the lines, from the tip of the arm. See Figure 1 for a visualization of the device, and Table I for the values of the parameters. We denote by $\alpha \in [0, 2\pi)$ the signed angle measured between the arm and the wind direction $\hat{\mathbf{x}}$, assumed constant and horizontal. We also assume the lines to be rigid and of constant length (positivity of the mechanical tension along the lines is verified *a posteriori*). We introduce the following vectors

$$\mathbf{a} = \mathbf{OA}, \mathbf{r} = \mathbf{OK}, \text{ and } \boldsymbol{\ell} = \mathbf{AK} \tag{1}$$

as well as the notation for unit vectors

$$\hat{\mathbf{x}} = \frac{\mathbf{x}}{\|\mathbf{x}\|}. \tag{2}$$

The kite is steered left and right by pulling the corresponding control line, while the tension in the lines is regulated by pulling or releasing both lines simultaneously. Under this

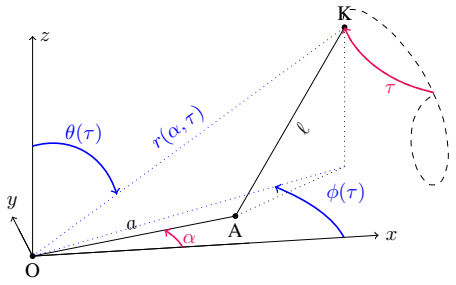


Fig. 1. Configuration of the system. The vector $\mathbf{OA}$ represents the arm, connected at point A (tip of the arm) to the kite K by the lines $\mathbf{AK}$.

Authorized licensed use limited to: INRIA. Downloaded on October 26,2026 at 15:07:52 UTC from IEEE Xplore. Restrictions apply.

actuation, the kite follows a prescribed lemniscate, see [6] with $\mathrm{Rot} = 0$ in our study, a path whose radial distance from the origin is free, so its trajectory lies on the conical hull of an eight-shaped curve (see Figure 2), with the origin as its vertex. As the kite sweeps along through this trajectory, it generates alternating lateral forces on the arm, causing the arm to oscillate. This oscillatory motion drives the electric generator coupled to the arm, converting the mechanical energy extracted from the wind into electrical power.

We introduce the unit vector $\hat{\mathbf{r}}$ pointing from the origin to the kite, whose evolution captures the prescribed lemniscate-shaped cone on which the kite moves. Its direction is determined by the variable $\tau \in [0, 2\pi)$:

$$\hat{\mathbf{r}} = \begin{pmatrix} \sin(\theta(\tau))\cos(\phi(\tau)) \\ \sin(\theta(\tau))\sin(\phi(\tau)) \\ \cos(\theta(\tau)) \end{pmatrix}. \tag{3}$$

The polar angle $\theta(\tau)$ and the azimuthal angle $\phi(\tau)$ are defined as:

$$\begin{aligned} \theta(\tau) &= \theta_0 + \Delta\theta \sin(2\tau) \\ \phi(\tau) &= \Delta\phi \sin(\tau) \end{aligned}. \tag{4}$$

As τ varies, the unit vector $\hat{\mathbf{r}}$ traces a lemniscate on the unit sphere. The shape of the lemniscate is parameterized by:

- θ_0, the mean polar angle, defining the position of the lemniscate center relative to the vertical (z-axis);
- $\Delta\theta$, the polar half-amplitude, defining the vertical opening angle (height) of the lemniscate;
- $\Delta\phi$, the azimuthal half-amplitude, defining its horizontal opening angle (width).

Given (α, τ), we compute r as

$$r = (\mathbf{a} \cdot \hat{\mathbf{r}}) + \sqrt{(\mathbf{a} \cdot \hat{\mathbf{r}})^2 + \ell^2 - a^2}, \tag{5}$$

thus, this pair of values entirely determines the configuration of the device. We therefore use $\mathbf{q} = (\alpha, \tau) \in S^1 \times S^1$ as the generalized coordinates for the system, and the state is $x = (\mathbf{q}, \dot{\mathbf{q}}) \in T(S^1 \times S^1)$.

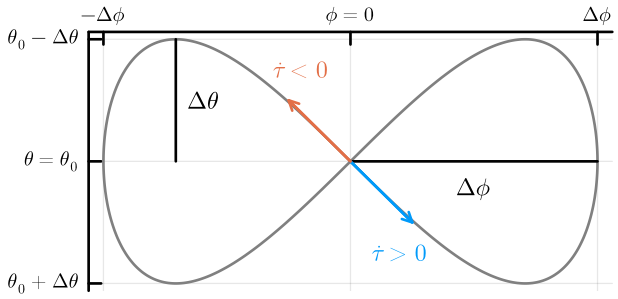


Fig. 2. The lemniscate, which forms the base of the kite's cone of constraints, is parameterized by τ and its shape is controlled by the design parameters θ_0, $\Delta\theta$, and $\Delta\phi$. Trajectories with increasing τ (blue) result in a flight path that ascends in the middle and descends at the sides, while decreasing τ (orange) produces the inverse motion. The y-axis is inverted to align with the orientation of the kite's trajectory.

B. Equations of motion

The forces acting on the kite are: the weight $\mathbf{F}_g$, line tension $\mathbf{F}_\ell = -F_\ell \hat{\boldsymbol{\ell}}$, aerodynamic forces $\mathbf{F}_a$. The weight is $\mathbf{F}_g = (m + m_\ell/2)\mathbf{g}$ with m and m_ℓ the mass of the kite and of the lines respectively, as we assume that half the weight of the lines is supported by the arm (this is strictly accurate only when the lines are horizontal and static). For the aerodynamic force, we consider a constant wind $\mathbf{w}(z) = w_0(z/z_0)^{1/7}\hat{\mathbf{x}}$, such that the wind speed is w_0 at the reference altitude z_0, and we denote $\mathbf{w}_a = \mathbf{w} - \dot{\mathbf{r}}$ the apparent wind. We compute the lift and drag of the kite, respectively

$$\begin{aligned} L &= \frac{1}{2} S \rho_a C_L \|\mathbf{w}_a\|^2 \\ D &= \frac{1}{2} S \rho_a C_D \|\mathbf{w}_a\|^2 \end{aligned} \tag{6}$$

where S is the surface of the kite, C_L and C_D its lift and drag coefficients, and ρ_a the density of the air. For a higher fidelity model, C_L and C_D should be functions of the angle of attack, the angle between the kite and the incoming airflow, but this is not modeled here; thus, these coefficients are constants. We approximate the drag of the lines with

$$\tilde{D}_\ell = \frac{1}{6} n \ell d_\ell \rho_a C_{D,\ell} \|\mathbf{w}_a\|^2, \tag{7}$$

where n is the number of lines, d_ℓ their diameter, and $C_{D,\ell}$ their drag coefficient. The computation leading to this approximation can be found in [1]. The resultant of the aerodynamic forces is finally given by

$$\mathbf{F}_a(\mathbf{q}, \dot{\mathbf{q}}) = L\hat{\mathbf{k}}_t + (D + \tilde{D}_\ell)\hat{\mathbf{k}}_b \tag{8}$$

where $\mathcal{B}_k = (\hat{\mathbf{k}}_b, \hat{\mathbf{k}}_r, \hat{\mathbf{k}}_t)$ (*back*, *right*, and *top* unit vectors, from the kite's perspective) is the body frame of the kite defined using the apparent wind as

$$\hat{\mathbf{k}}_b = \frac{\mathbf{w}_a}{\|\mathbf{w}_a\|}, \quad \hat{\mathbf{k}}_r = \frac{\hat{\boldsymbol{\ell}} \times \hat{\mathbf{k}}_b}{\left\|\hat{\boldsymbol{\ell}} \times \hat{\mathbf{k}}_b\right\|}, \text{ and } \hat{\mathbf{k}}_t = \hat{\mathbf{k}}_b \times \hat{\mathbf{k}}_r, \tag{9}$$

as in [5].

We determine an expression for $\mathbf{F}_\ell$ using Newton's second law on the rotating arm of inertia I. The generator has a torque function linear with respect to its angular velocity $\dot{\alpha}$ and is parameterized by a braking coefficient b, such that

$$T(\dot{\alpha}) = -b\,\dot{\alpha}, \tag{10}$$

and the lines apply a moment $M_\Delta(-\mathbf{F}_\ell)$ to the arm, with $\Delta = (O, \hat{\mathbf{z}})$ the axis of rotation of the arm. We compute

$$M_\Delta(-\mathbf{F}_\ell) = aF_\ell \hat{\boldsymbol{\ell}} \cdot (\hat{\mathbf{z}} \times \hat{\mathbf{a}}). \tag{11}$$

Newton's second law gives

$$I\ddot{\alpha} = M_\Delta(-\mathbf{F}_\ell) + T(\dot{\alpha}), \tag{12}$$

from which we compute

$$\mathbf{F}_\ell = \frac{-I\ddot{\alpha} - b\dot{\alpha}}{a\hat{\boldsymbol{\ell}} \cdot (\hat{\mathbf{z}} \times \hat{\mathbf{a}})} \hat{\boldsymbol{\ell}}. \tag{13}$$

The kite is controlled through an aerodynamic force obtained by pulling the lines in a specific way. We introduce

Authorized licensed use limited to: INRIA. Downloaded on October 26,2026 at 15:07:52 UTC from IEEE Xplore. Restrictions apply.

directly this force $\mathbf{F}_c$, the analogue of the sideways force the rails would exert on a train to steer it, and isolate it in the equation given by Newton's second law applied to the kite's center of mass:

$$\mathbf{F}_c(\mathbf{q}, \dot{\mathbf{q}}, \ddot{\mathbf{q}}) = m\ddot{\mathbf{r}}(\mathbf{q}, \dot{\mathbf{q}}, \ddot{\mathbf{q}}) - \mathbf{F}_g - \mathbf{F}_a(\mathbf{q}, \dot{\mathbf{q}}) - \mathbf{F}_\ell(\mathbf{q}, \dot{\mathbf{q}}, \ddot{\mathbf{q}}). \tag{14}$$

Given a certain position and velocity, we find that $\mathbf{F}_c$ must adhere to the following system of equations for the kite to glide on the lemniscate cone without friction:

$$\begin{cases} \mathbf{F}_c \cdot \frac{\partial \mathbf{r}}{\partial r} = 0 \\ \mathbf{F}_c \cdot \frac{\partial \mathbf{r}}{\partial \tau} = 0, \end{cases} \tag{15}$$

with $\mathbf{r}(\alpha, \tau) = r(\alpha, \tau)\hat{\mathbf{r}}(\tau)$. We work on this system and, using all previous equations, we determine $A(\mathbf{q})$ (an invertible 2×2 matrix) and $\mathbf{b}(\mathbf{q}, \dot{\mathbf{q}})$ such that

$$A(\mathbf{q})\ddot{\mathbf{q}} = \mathbf{b}(\mathbf{q}, \dot{\mathbf{q}}). \tag{16}$$

The computation of A and $\mathbf{b}$ is fully detailed in [1].

Remark: This dynamical system exhibits the following symmetry

$$(\alpha, \tau) \mapsto (-\alpha, \tau + \pi), \tag{17}$$

which reflects the configuration in 3D space about the plane $(O, \hat{x}, \hat{z})$.

TABLE I
PARAMETER DESCRIPTION AND VALUES

Symbol	Description	Value	Unit
a	Arm length	2	m
b	Arm braking coefficient	4000	$\mathrm{N\,m\,s\,rad^{-1}}$
C_D	Kite drag coefficient	$C_L/7$	
$C_{D,\ell}$	Line drag coefficient	0	
C_L	Kite lift coefficient	0.6	
d_ℓ	Line diameter	0.003	m
g	Gravity	9.81	$\mathrm{m\,s^{-2}}$
I	Arm inertia	1300	$\mathrm{kg\,m^2}$
ℓ	Line length	31	m
m	Kite mass	6	kg
S	Kite surface	10	$\mathrm{m^2}$
w_0	Wind reference speed	9	$\mathrm{m\,s^{-1}}$
z_0	Wind reference altitude	10	m
$\Delta\theta$	Lemniscate polar half-height	$6\pi/180$	rad
$\Delta\phi$	Lemniscate azimuthal half-width	$50\pi/180$	rad
θ_0	Lemniscate mean polar angle	$65\pi/180$	rad
ρ_a	Air density	1.225	$\mathrm{kg\,m^{-3}}$
ρ_ℓ	Line density	707	$\mathrm{kg\,m^{-3}}$

III. EQUILIBRIA AND LIMIT CYCLES

A. Preliminary numerical simulations

We implement 16 in Julia using ForwardDiff.jl [8] for automatically computing derivative expressions like $\ddot{\mathbf{r}}(\mathbf{q}, \dot{\mathbf{q}})$, and DifferentialEquations.jl [7] which provides Tsit5, a Runge-Kutta scheme of order 5 with adaptive step size and dense output.

Starting from two initial states $\mathbf{x}^0 = (0, \pm 1, 0, 0)$, the kite trajectories converge toward two distinct limit cycles.

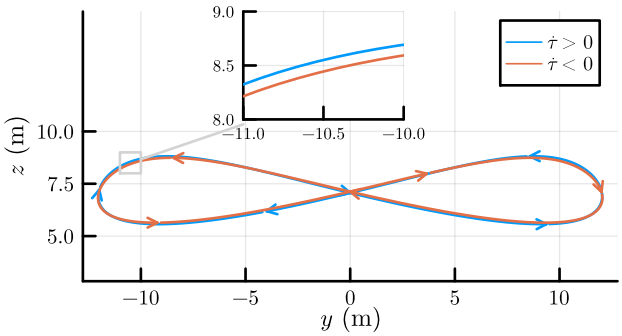


Fig. 3. Projection of the kite trajectories onto the YZ plane for the two limit cycles with opposite directions of motion (arrows indicate the direction of the kite motion). Zooming in on the trajectories shows that the two paths are distinct.

While both follow a lemniscate shape, they are traversed in opposite directions and occupy different paths in 3D space, see Figure 3. In this study, we focus exclusively on the side-ascending trajectories, characterized by $\dot{\tau} > 0$, as the other direction leads to line tangling and premature wear.

B. Convergence toward the limit cycle

We define a sequence of states $(\mathbf{x}_i)_{i \geq 1}$ lying on a surface of section Σ, such that $\mathbf{x}_{i+1}$ is the first intersection between $\{\varphi^t(\mathbf{x}_i),\, t > 0\}$ and Σ, where φ^t is the flow of (16). Let

$$\Sigma = \{\mathbf{x} \in T(S^1 \times S^1) \mid \tau(\mathbf{x}) = 0\} \tag{18}$$

and $\Delta t(\mathbf{x})$ be the time needed to achieve the first crossing of Σ from state $\mathbf{x}$, namely:

$$\Delta t(\mathbf{x}) = \min\{t > 0 \mid \varphi^t(\mathbf{x}) \in \Sigma\}. \tag{19}$$

We then define the first recurrence map, or Poincaré map, as

$$P : \mathbf{x} \in T(S^1 \times S^1) \mapsto \varphi^{\Delta t(\mathbf{x})}(\mathbf{x}) \in \Sigma, \tag{20}$$

and finally the desired sequence

$$\begin{cases} \mathbf{x}_0 = P(\mathbf{x}^0) \\ \mathbf{x}_{i+1} = P(\mathbf{x}_i). \end{cases} \tag{21}$$

Since the trajectory starting at $\mathbf{x}^0$ approaches an attracting limit cycle, the limit of this sequence is defined and we plot the distance from $\mathbf{x}_i$ to $\mathbf{x}_\infty = \lim_{i \to \infty} \mathbf{x}_i$ in Figure 4. The sequence converges exponentially, and in only 7 iterations (seven revolutions over the lemniscate), we reach the precision limit of our ODE solver, with a distance of less than 10^{-12}; in fact, we approximately gain 2 digits of $\mathbf{x}_\infty$ after each revolution. The points $\mathbf{x}_i$ are obtained using DifferentialEquations.jl's continuous callback feature, which saves the current state when a user defined function changes its sign, using the high-precision dense output from the ODE solver.

We confirm that there exist only two attracting limit cycles by sampling the state space with $(\alpha, \tau) \in S^1 \times S^1$ and velocities $-M \leq \dot{\alpha}, \dot{\tau} \leq M$, and simulating the trajectory of each sampled point until convergence to a limit cycle with

Authorized licensed use limited to: INRIA. Downloaded on October 26,2026 at 15:07:52 UTC from IEEE Xplore. Restrictions apply.

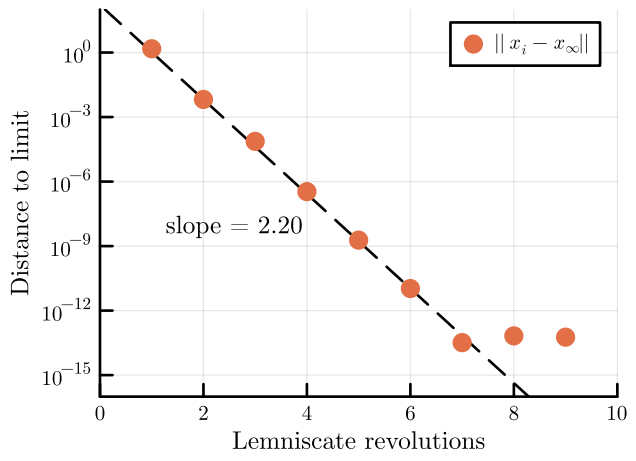


Fig. 4. Convergence toward the limit cycle. The trajectory gets closer to the limit cycle as the number of lemniscate revolutions (a revolution is defined as a sweep over the interval $[0, 2\pi]$ for the angle τ) increases. The linear trend in log-linear plot indicates exponential convergence; after each revolution, the distance to the limit decreases by a factor of $10^{2.20}$, until it stalls near the tolerance of the integration scheme.

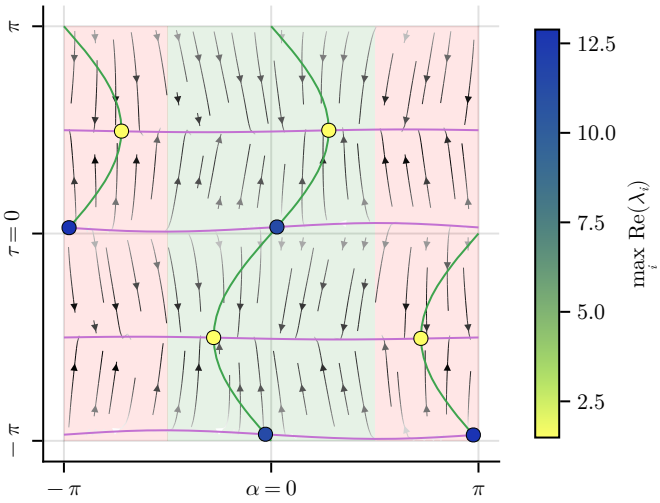


Fig. 5. Zero velocity curves and equilibria of the dynamics. The black arrows represent the direction of the vector field $\ddot{\mathbf{q}}(\mathbf{q}, \dot{\mathbf{q}} = 0)$, the green lines are the nullclines of $\ddot{\alpha}(\alpha, \tau)$, *i.e.* the points (α, τ) such that $\ddot{\alpha}(\alpha, \tau) = 0$, and the purple lines are the ones of $\ddot{\tau}(\alpha, \tau)$. At their intersections lie the equilibria of the system (all unstable), with color codes ranging from yellow to blue according to the highest real part of their eigenvalues. The background is green when the arm points downwind and red when it points upwind.

a 1×10^{-9} tolerance. We choose $M = 10 \mathrm{rad\,s^{-1}}$ as upper bound; it corresponds to extreme arm and kite speeds which would be quickly damped by the generator and aerodynamic drag anyway.

C. Equilibria

Starting from an equilibrium, we can reach either of the two limit cycles for any set of parameters by adding a small perturbation to $\dot{\tau}$ with the corresponding sign. A state $\mathbf{x} = (\mathbf{q}, \dot{\mathbf{q}})$ is an equilibrium if $\dot{\mathbf{x}} = (\dot{\mathbf{q}}, \ddot{\mathbf{q}}) = 0 \in \mathbb{R}^4$. To find an equilibrium, we thus look for a solution $\mathbf{q}$ to $\ddot{\mathbf{q}}(\mathbf{q}, \dot{\mathbf{q}} = 0) = 0$. In Figure 5, we plot the nullclines for $\ddot{\mathbf{q}}$ and show the equilibria. We are more interested in the behavior of the system in the green region, where the arm points downwind, to leave a safe area upwind of the device. They are all unstable; thus, we can choose any of them, set its $\dot{\tau}$ component to a small positive value (for the limit cycle with $\dot{\tau} > 0$) and integrate for ten revolutions to ensure the limit cycle is reached.

IV. LIMIT CYCLE OPTIMIZATION

A. Optimizing for maximum average power

In this section, we maximize the average power over a limit cycle by tuning a selection of design parameters. To assess the quality of a set of parameters, we measure the total work done by the generator, *i.e.* the amount of energy extracted from the system. We obtain this information by augmenting the state with the work W done since the start of the simulation, whose time derivative is the instantaneous power:

$$\dot{W} = P = -\dot{\alpha}\, T(\dot{\alpha}) \geq 0, \tag{22}$$

and we denote the augmented state $\tilde{\mathbf{x}} = (\mathbf{x}, W)$. We maximize the average power W_f/t_f over one limit cycle, whose orientation is chosen by setting either $\tau_f = 2\pi$ or $\tau_f = -2\pi$; we choose the former. The optimization problem then reads

$$W_f/t_f \underset{\substack{\alpha_0, \dot{\alpha}_0, \dot{\tau}_0 \\ W_f, t_f \\ \Theta}}{\longrightarrow} \max \tag{23}$$

subject to constraints

$$\begin{aligned} \alpha(t_f, \Theta) &= \alpha_0 \\ \tau(t_f, \Theta) &= \tau_f \\ \dot{\alpha}(t_f, \Theta) &= \dot{\alpha}_0 \\ \dot{\tau}(t_f, \Theta) &= \dot{\tau}_0 \\ W(t_f, \Theta) &= W_f, \end{aligned} \tag{24}$$

where the components of $\tilde{\mathbf{x}}(t_f, \Theta)$ are obtained by integrating $\tilde{\mathbf{x}}_0 = (\alpha_0, 0, \dot{\alpha}_0, \dot{\tau}_0, 0)$ with optimized parameters Θ. We reuse our work on equilibria and limit cycles to provide the solver with an initial guess that satisfies the constraints. We solve this problem using the interior point method implemented by Ipopt [9] with linear solver MUMPS [10]; we use ForwardDiff.jl again [8] for algorithmically computing the derivatives needed during the optimization. The parameters and their bounds are described in Table II while the result of the optimization is presented in Table III. We show the power curve over the limit cycle in Figure 6. Ipopt converges within 11 iterations (0.5 s on an M2 MacBook Air) for a required tolerance of 10^{-6}.

B. Optimal design as a function of wind speed

Since the optimization converges quickly, we repeat the procedure for a range of reference wind speeds, w_0. For each integer wind speed from $5\,\mathrm{m\,s^{-1}}$ to $15\,\mathrm{m\,s^{-1}}$, we find the set of parameters (Figure 9) that maximizes power (Figure 7) and show the corresponding minimum and maximum line

Authorized licensed use limited to: INRIA. Downloaded on October 26,2026 at 15:07:52 UTC from IEEE Xplore. Restrictions apply.

TABLE II

DESCRIPTION OF THE OPTIMIZED PARAMETERS

Symbol (Unit)	Lower	Upper
ℓ (m)	10.3	93.0
I (kg m^2)	433.3	3900.0
b (N m rad^{-1} s^{-1})	1333.3	12 000.0

TABLE III

OPTIMIZATION RESULTS

Symbol (Unit)	Initial Guess	Solution
ℓ (m)	31.0	47.4
I (kg m^2)	1300.0	3541.3
b (N m rad^{-1} s^{-1})	4000.0	3862.6
Average power (kW)	9.05	10.21
Norm of residual	3.7×10^{-9}	5.3×10^{-10}

tension over the limit cycle (Figure 8). For comparison, we also compute the power and line tension extrema using the set of parameters obtained in Section IV-A optimized for a wind speed of $10\,\mathrm{m\,s^{-1}}$. This set of parameters proves strongly resilient across a wide range of wind speeds ($\pm 50\%$) as it yields nearly as much power as the actual optimum (with a difference of less than 5%), showing only a slight increase in tension. The system exhibits quasilinear scaling along this parameterized optimization even though the length of the arm is kept constant (and other parameters), thus making it impossible to perfectly scale the model to wind speed. We observe the following approximate trends:

- power is proportional to the cube of wind speed; this is consistent with the scaling of wind power,
- tension is proportional to the square of wind speed,
- line length ℓ and arm inertia I are both ratios of first order polynomials in wind speed,
- arm braking coefficient b is proportional to wind speed,
- (not shown) the period is inversely proportional to wind speed.

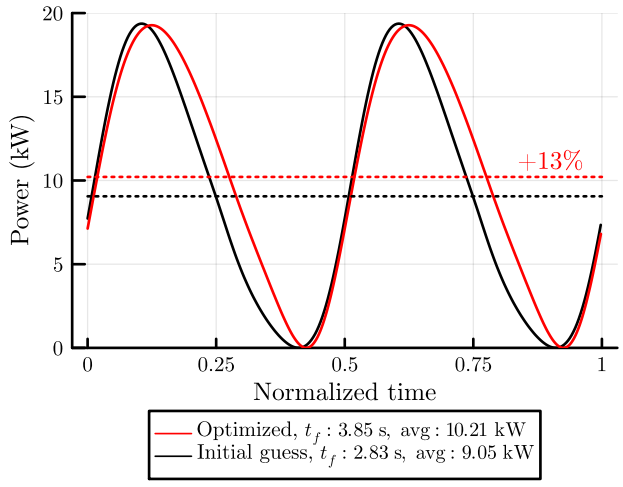


Fig. 6. Power generation curves over the normalized time comparing the initial guess (black) to the optimized limit cycle (red). Solid lines represent instantaneous power, while the horizontal dotted lines indicate the average power generated over the cycle. After optimization, the period is significantly increased, resulting in approximately 13% more power harvested on average.

The maximum line tension defines the strength requirements for the kite fabric and lines. Furthermore, the minimum line tension remains positive, confirming *a posteriori* the modeling assumption that the lines are always in tension and never exert compression on the arm.

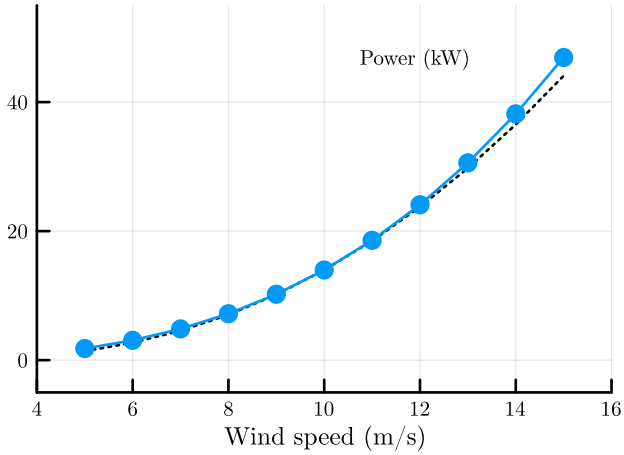


Fig. 7. Average generated power for optimized (blue) and reference (black) parameters when the reference wind speed w_0 is varied. The reference curve is generated by fixing the design parameters to the optimal values for a $w_0 = 10\,\mathrm{m\,s^{-1}}$.

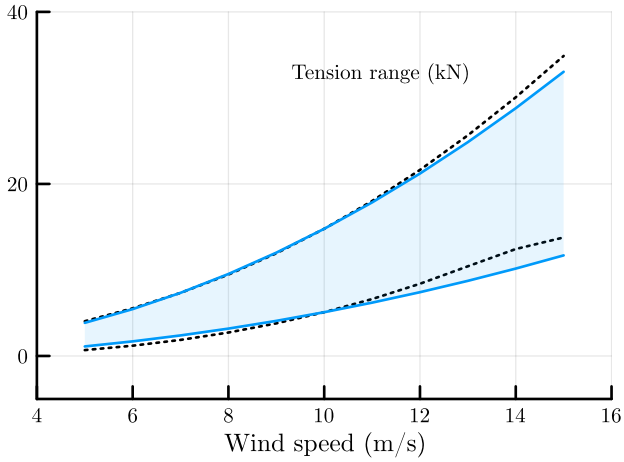


Fig. 8. Minimum and maximum line tension $\mathbf{F}_\ell$ for optimized (blue) and reference (black) parameters.

V. CONCLUSION

A novel airborne wind energy system has been presented and analyzed. By following a periodic lemniscate trajectory, the kite exerts a pulling force on the arm, causing oscillations that are transformed into electrical energy. This

Authorized licensed use limited to: INRIA. Downloaded on October 26,2026 at 15:07:52 UTC from IEEE Xplore. Restrictions apply.

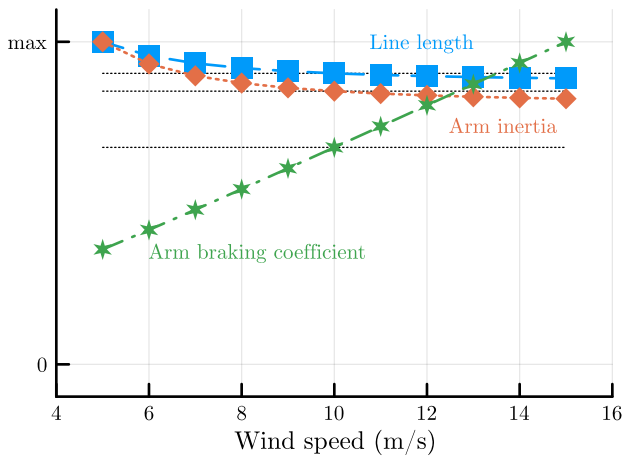


Fig. 9. Optimal parameters for each wind speed (color) and and reference parameters fixed at the optimum for $w_0 = 10\,\mathrm{m\,s^{-1}}$ (black dashed lines).

ground-generation configuration with a moving ground station represents a simplified and potentially more efficient alternative to existing airborne wind energy technologies. A novel modeling approach has been developed to analyze this system. Rather than explicitly modeling the control actions on the kite, an implicit formulation has been adopted where the kite's position is constrained to lie on a prescribed figure-eight pattern. This approach transforms the complex control problem into a differential algebraic equation that can be reduced to a four-dimensional ordinary differential system. The resulting ODE depends on several design parameters including line length, arm inertia, and braking coefficient, enabling systematic parametric analysis and optimization. Specific equilibrium points serve as starting configurations for numerical continuation methods, allowing the computation of physically relevant limit cycles. This systematic approach provides robust initial guesses that are essential for the subsequent optimization process, avoiding convergence to non-physical or suboptimal solutions. This optimization of design parameters with respect to average power generation has demonstrated significant performance improvements. Compared to baseline parameter values, the optimized configuration yields approximately a 13% increase in generated power while maintaining positive line tension throughout the cycle. Furthermore, extensive analysis across reference wind speeds ranging from $5\,\mathrm{m\,s^{-1}}$ to $15\,\mathrm{m\,s^{-1}}$ has revealed remarkable robustness of the optimized parameters. The system exhibits nearly linear scaling properties with wind speed, and parameters optimized for $10\,\mathrm{m\,s^{-1}}$ perform near-optimally across the entire wind speed range.

This simplified model serves as a valuable foundation for ongoing research. While the implicit control formulation enables efficient analysis and optimization, future work will incorporate explicit control modeling to capture the actual actuation mechanisms of the kite. The limit cycles and optimal parameters identified in this study provide excellent initialization for more sophisticated optimal control frameworks such as AWEbox [3]. Additionally, the model is directly applicable to prototype design and dimensioning, offering practical utility beyond its theoretical contributions.

ACKNOWLEDGMENT

The authors wish to very warmly thank their colleagues C. Jochum and J.-B. Leroux from ENSTA for many fruitful exchanges on this topic.

REFERENCES

[1] A. Bavoil. Rapport technique du projet KEEP. Technical report, *Université Côte d'Azur*, April 2024. `https://hal.science/hal-04513387`

[2] A. Cherubini, A. Papini, R. Vertechy, and M. Fontana. Airborne wind energy systems: A review of the technologies. *Renewable and Sustainable Energy Reviews*, 51:1461–1476, 2015.

[3] J. De Schutter, R. Leuthold, T. Bronnenmeyer, E. Malz, S. Gros, and M. Diehl. AWEbox: An optimal control framework for single- and multi-aircraft airborne wind energy systems. *Energies*, 16(4):1900, 2023.

[4] R. van der Vlugt, A. Bley, M. Noom, and R. Schmehl. Quasi-steady model of a pumping kite power system. *Renewable Energy*, 131:83–99, 2019.

[5] L. Fagiano, M. Milanese, and D. Piga. High-altitude wind power generation. *IEEE Transactions on Energy Conversion*, 25(1):168–180, 2010.

[6] M. Ahmed, A. Hably, and S. Bacha. Power maximization of a closed-orbit kite generator system. *50th IEEE Conference on Decision and Control and European Control Conference (CDC-ECC)*, pages 7717–7722, Orlando, FL, USA, 2011. IEEE.

[7] C. Rackauckas and Q. Nie. DifferentialEquations.jl — a performant and feature-rich ecosystem for solving differential equations in Julia. *Journal of Open Research Software*, 5(1), 2017.

[8] J. Revels, M. Lubin, and T. Papamarkou. Forward-mode automatic differentiation in Julia. *arXiv:1607.07892 [cs.MS]*, 2016.

[9] A. Wächter and L. T. Biegler. On the implementation of an interior-point filter line-search algorithm for large-scale nonlinear programming. *Mathematical Programming*, 106(1):25–57, 2006.

[10] P. R. Amestoy, I. S. Duff, J. Koster, and J.-Y. L'Excellent. A fully asynchronous multifrontal solver using distributed dynamic scheduling. *SIAM Journal on Matrix Analysis and Applications*, 23(1):15–41, 2001.

Authorized licensed use limited to: INRIA. Downloaded on October 26,2026 at 15:07:52 UTC from IEEE Xplore. Restrictions apply.